J. Fluid Mech. (2024), *vol*. 998, A38, doi:10.1017/jfm.2024.826

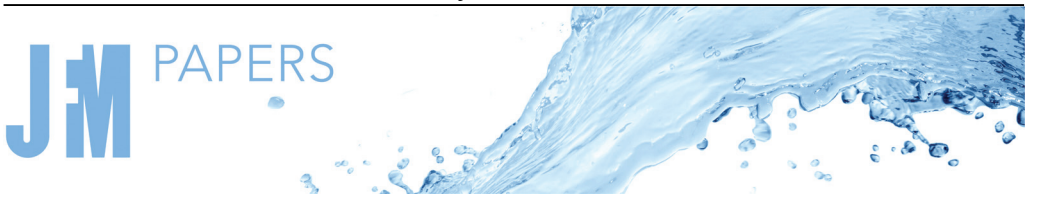

Regular reflection to Mach reflection (RR–MR) transition in short wedges

Vinod Yeldho Baby[1], **Vinoth Paramanantham**[1] **and G. Rajesh**[1],†

[1]Indian Institute of Technology Madras, Chennai 600036, India

(Received 10 July 2023; revised 19 August 2024; accepted 24 August 2024)

Regular reflection (RR) to Mach reflection (MR) transitions (RR ↔ MR) on long wedges in steady supersonic flows have been well studied and documented. However, in a short wedge where the wedge length is small, the transition prediction becomes really challenging owing to the interaction of the expansion fan emanating from the trailing edge of the wedge with the incident shock and the triple/reflection point. The extent of this interaction depends on the distance between the wedge trailing edge and the symmetry line (Ht). This distance is a geometric combination of the distance of the wedge leading edge from the symmetry line (H), the wedge angle (θ) and the wedge length (w). In the present study, we used the method of characteristics to model the complete wave interactions which accurately predicted shock curvatures and the reflection configurations for all ranges of the incoming flow Mach number. In the case of short wedges, the transition criterion strongly depends on the wedge length, which can be so adjusted even to eliminate the RR → MR transitions till the wedge angle reaches the no-reflection domain. Transition lines for both the detachment criterion and von Neumann criterion are also drawn to investigate the dual solution domain, and the reflection configurations were verified experimentally for the first time on short wedges. By using proper input configuration parameter (w/H), various types of shifts in the dual solution domain for short wedges are studied and categorised into three types, namely Type I, Type II and Type III.

Key words: shock waves, supersonic flow

1. Introduction

When a supersonic flow passes over symmetric wedges, a shock interaction/reflection occurs due to the flow turning. The shock reflection can be either a Mach reflection

† Email address for correspondence: rajesh@ae.iitm.ac.in

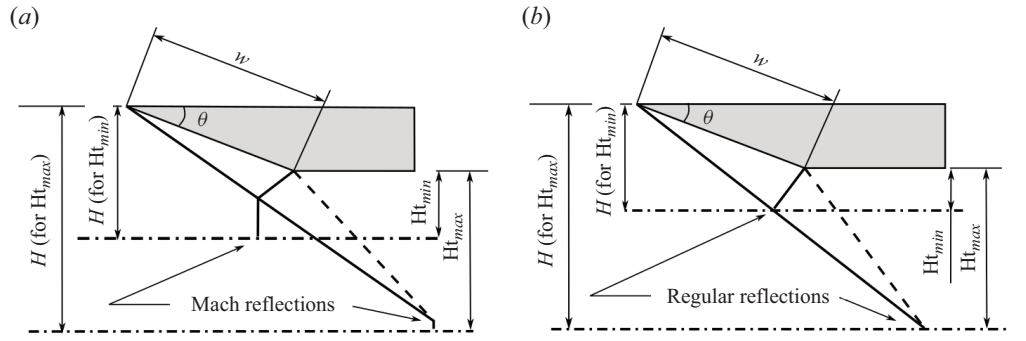

Figure 1. Ht_{min} and Ht_{max} for (*a*) MR and (*b*) RR.

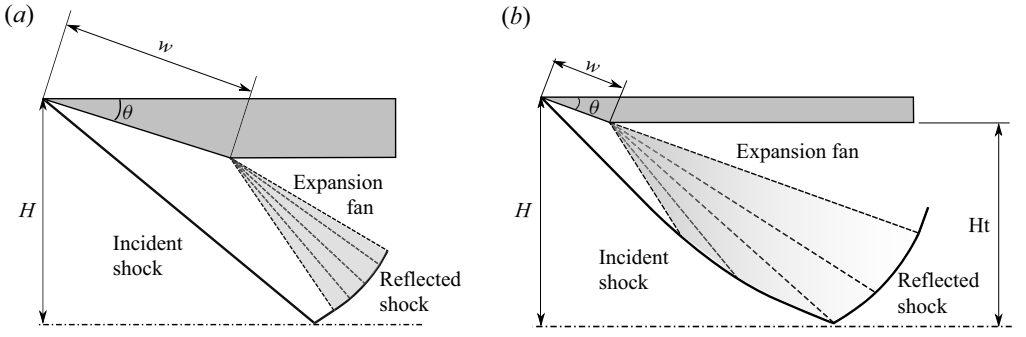

Figure 2. Schematic diagram for (*a*) long wedge and (*b*) short wedge.

(MR) or a regular reflection (RR), depending on the flow parameters and wedge geometry. Figure 1 depicts the possible shock reflections between the maximum and minimum values of the height of the trailing edge from the symmetry line (Ht) (Li & Ben-Dor 1997). The Ht value depends on the wedge length (w), wedge angle (θ) and the height of the wedge leading edge from the symmetry line (H), as shown in figure 1(*a*,*b*). The wedge length is also an essential parameter, and based on the non-dimensionalised wedge length (w/H), we can classify wedges as long or short. As depicted in figure 2(*a*), most research on wedge flow focuses on long wedges where the expansion fan from the trailing edge does not interact with the incident shock wave. As shown in figure 2(*b*), the expansion fan will interact with the incident shock wave in the short wedges. Due to expansion fan interaction, the incident shock angle in short wedges decreases, and the shock curves continuously from the point where the leading expansion characteristic meets the shock wave to the triple/reflection point.

The curvature of the incident shock essentially depends on the extent of the expansion fan interaction. Consequently, the incident shock angle at the point of reflection will depend not only on the wedge angle and the flow Mach number but also on the w/H ratio. Any attempt to predict the shock transitions on short wedges must hence incorporate an accurate model of the incident shock curvature resulting from its interaction with the expansion fan.

1.1. *Previous works in shockwave – expansion fan interaction*

The interaction of shock waves and expansion waves in one-dimensional flows is the subject of several investigations in high-speed flows (Emanuel 2001). A comprehensive description of the interaction of shock waves, expansion waves and contact surfaces,

mainly in shock tube flows, can be seen in the work of Glass (1991). Li & Ben-Dor (1996) conducted a study on the interaction between expansion fans and shock waves in symmetric wedge flows. In this work, Li & Ben-Dor (1996) developed an analytical model to obtain the curvature of the shock wave due to its interaction with the centred expansion wave of the opposite family by using a second-order polynomial. The experimental and numerical validations of this analytical model (Nel & Skews 2019) revealed that while the model prediction was accurate for small interactions, it could not predict shock curvature for stronger interactions. Vuillon, Zeitoun & Ben-Dor (1995) numerically studied the RR $\leftrightarrow$ MR transitions in the dual solution domain and found that the Mach stem height reduced linearly as the wedge trailing-edge height is increased. From numerical simulations, they also found a value of the trailing edge height Ht_{tr} in between Ht_{max} and Ht_{min}. They concluded that when the Ht value is in between Ht_{tr} and Ht_{max}, the stable configurations were regular reflections and the numerical attempts to establish Mach reflection configurations in this range failed. However, later, Li & Ben-Dor (1997) found out that the equation used by Vuillon *et al.* (1995) to calculate Ht_{max} was wrong due to an incorrect assumption and corrected this. Moreover, Vuillon *et al.* (1995) have not considered the transition phenomenon when the expansion fan starts interacting with the incident shock which is the context of the present study. In another study by Hillier (2007) on the shock-wave/expansion-wave interaction and the transition between regular and Mach reflections, analytical and numerical simulations were carried out to investigate the inviscid interactions of an expansion wave with an incident shock wave of the opposite family. The study was to stabilise a Mach reflection in a parallel duct for different flow conditions. Most of the analytical methods developed in shock reflections focused on predicting the MR configuration and the Mach stem height, a finite length scale in an MR in long wedges (Azevedo & Liu 1993; Li & Ben-Dor 1997; Mouton & Hornung 2007). In these models, the slip line, which originates from the triple point in a Mach reflection, was assumed to be a straight line. Later, the refinement of the slip line curvature was carried out (Gao & Wu 2010; Bai & Wu 2017) resulting in a better Mach stem prediction, as they considered the expansion waves generated over the slip line and its interaction with the transmitted expansion waves through the reflected shock. Further, numerical studies of a shock reflection in the presence of an upstream expansion wave and a downstream shock wave for two-dimensional flows by Yao, Li & Wu (2013) reported that the expansion fan delayed the RR $\leftrightarrow$ MR transition at lower Mach numbers ($M = 2$–3.5) and expedited it at higher Mach numbers.

The analytical models discussed above were all for the interaction of the shock wave with the opposite (either right-running or left-running) family of expansion waves. In contrast, the incident shock in short wedges is curved as a result of the prolonged interaction of the expansion wave of the same family. The study of this type of interaction is significant because the RR $\leftrightarrow$ MR transition may only depend on the incident shock angle at the reflection point, which is determined by the shock curvature caused by the interaction. As a result, it is critical to identify the parameters that govern the shock angle at the reflection point, as well as the changes in transition criteria that occur when these parameters change.

Bai (2023) conducted the first analytical and computational studies of the incident shock interaction with the wedge trailing-edge expansion fan of the same family. The shock reflection transitions were quantified for different values of g (wedge trailing-edge height to inlet height (Ht/H), as shown in figure 2*b*). Bai (2023) developed an analytical model to predict incident shock wave curvature due to expansion wave interaction. The model is based on the interaction of C$-$ waves generated from the wedge trailing edge and neglects the reflected C+ characteristics from the interaction point. For short wedges, the shift in the

detachment and von Neumann transition lines for various g values were also constructed by Bai (2023). Apart from that, the results for Mach numbers less than two were not provided (refer to figure 6 of Bai 2023). For a given M and θ_w value, the $g^{(D)}$ value or $g^{(N)}$ value is found out from the above-mentioned plot of Bai (2023) and then this value is compared with the calculated g value to determine whether the shock reflection is an MR or an RR. Although the analytical method is very fast, ignoring the C+ waves in the model assumption may lead to small errors at higher wedge angles especially close to the no-reflection boundary.

In addition to the model of Bai (2023), there is another model that approximates the interaction between shock waves and expansion waves. In 1952, Moeckel (1952) introduced a method for determining the shockwave curvature in a non-uniform flow field, particularly for an upstream flow characterised by a Mach number that changes continuously. Moeckel (1952) elaborated on the diverse possible interactions that can occur within the flow field and presented analytical frameworks for modelling the flow field, encompassing the interaction between the expansion fan and the shock wave (i.e. either upstream or downstream of the flow). Chisnell (1955) studied the interaction of a shock wave with a weak contact discontinuity and gave a first-order relationship between change in shock strength and change in density across the discontinuity, which is integrated to give the shock strength as a function of the initial density of the non-uniform medium in closed form. Subsequently, Whitham (1958) demonstrated that the works of Moeckel (1952) regarding the interaction of an oblique shock wave with a shear layer in steady supersonic flow and Chisnell (1955) regarding the propagation of a shock wave down a non-uniform tube are necessarily the same and named it as the Moeckel–Chisnell (MC) method. In the present work, we have applied the MC method to study the shock wave and expansion fan interaction.

In the MC method, the interaction between the expansion fan and the shockwave presents a formidable challenge, rendering it as computationally intensive as that of the method of characteristics (MoC). The inclusion of upstream interaction effects in the MC method for computing shockwave curvature does not result in substantial additional complexity. However, Moeckel (1952) showed that effective incorporation of downstream interactions of the expansion fan requires an iterative approach akin to that of MoC. Following this, Moeckel (1952) demonstrated that the shockwave curvature can be calculated with minimal error if the influence of reflected first-order waves caused by the downstream expansion fan interacting with the shockwave is ignored. This approximation, i.e. neglecting the first-order reflected waves, is used in developing the shockwave expansion fan interaction model in the present work along with a more precise MoC model. Similar assumptions were successfully used in the development and application of the shock-expansion theory. The magnitude of the error associated with this approximation grows with the increase in wedge angle and Mach number. In terms of error, the Mach number has a more significant impact than the wedge angle. The application of the approximations above in constructing a model for the current study is discussed in § 2.

In the current study, a semi-analytical model is developed using MoC equations and numerical techniques (henceforth referred to as the MoC method throughout this paper), which includes the reflected C+ waves from the incident shock, in contrast to the model of Bai (2023), which only considers C− waves to determine the incident shock curvature and shock angle at the reflection point. This MoC model is used to study the prolonged interaction of an expansion wave with an incident shock wave of the same family to predict the shock wave curvature. The MoC model developed is compared with the model of Bai (2023) and the MC method. Investigations on the shock transition in symmetric short

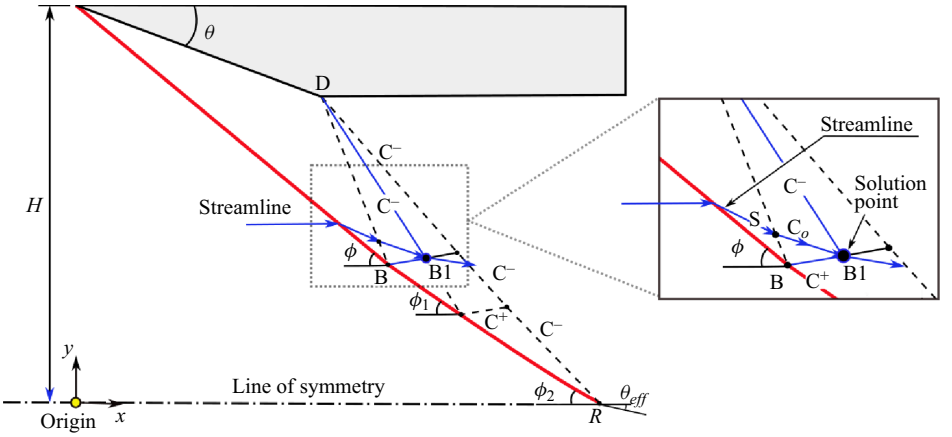

Figure 3. Shock–expansion fan interaction model using MoC.

wedges, particularly the shift in the dual solution domain, are also incorporated. We have used the w/H ratio as the independent parameter for studying the transition for a range of Mach numbers from 1 to 5, which led to three distinct classifications for the shock transitions in short wedges, in dual solution domains.

The MoC model is compared with a well-validated in-house computational fluid dynamics (CFD) model, which is an inviscid, two-dimensional (2-D), structured finite volume solver with a fifth-order WENO scheme (Paramanantham, Janakiram & Gopalapillai 2022). The RR $\leftrightarrow$ MR transition lines are expected to be altered by the interactions of the expansion wave with the shock wave due to the small wedge lengths. The reflections above and below the transition lines for short wedges are verified by comparing them with shadowgraph images from experiments.

2. Shock wave expansion fan interaction – analytical modelling

The MC method and MoC are employed to model the shockwave/expansion fan interaction, and the MoC results are compared to validate the accuracy of the MC model. In this section, we will examine the development of the MoC and MC methods for shock expansion interaction.

2.1. *Method of characteristics*

The shock–expansion interaction is modelled with the MoC which is clearly explained by Zucrow & Hoffmann (1977) for steady, two-dimensional rotational flow. The model assumptions are that the flow is steady, compressible, inviscid, two-dimensional (planar) and rotational as it is a curved shock. The entropy is constant only along the streamlines. The basic configuration of the incident shock–expansion fan interaction model is shown in figure 3. The characteristic and compatibility equations for two-dimensional, isentropic, rotational and supersonic flow are given in table 1. The details of the variables in table 1 and their implementation are explained in Appendix A in detail.

2.1.1. *Interior points*

The initial value line for the MoC is the first characteristic expansion line from the trailing edge (point D in figure 3), which terminates at the intersection of the incident shock wave

Characteristic equations	
$(\mathrm{d}y/\mathrm{d}x) = \lambda_0 = v/u$	(Streamline)
$(\mathrm{d}y/\mathrm{d}x) = \lambda_+ = \tan(\alpha + \mu)$	(Right running characteristic line, '+' subscript)
$(\mathrm{d}y/\mathrm{d}x) = \lambda_- = \tan(\alpha - \mu)$	(Left running characteristic line, '−' subscript)
Compatibility equations	
$\rho V\,\mathrm{d}V + \mathrm{d}\rho = 0$	(Streamline)
$\mathrm{d}p - a^2\,\mathrm{d}\rho = 0$	(Streamline)
$\frac{\sqrt{(M^2-1)}}{(\rho V^2)}\mathrm{d}p_+ + \mathrm{d}\alpha_+ = 0$	(Right running characteristic Mach, '+' subscript)
$\frac{\sqrt{(M^2-1)}}{(\rho V^2)}\mathrm{d}p_- - \mathrm{d}\alpha_- = 0$	(Left running characteristic line, '−' subscript)

Table 1. Steady, two-dimensional, isentropic, rotational supersonic flow.

and the first expansion line (point B). The solution algorithm is initiated by giving a small increment of flow turn angle downstream from point D. The flow properties at point D are determined using the Prandtl–Meyer relations. The C− curve from point D and the C+ curve from point B intersect at point B1 as shown in figure 3. The rearward running streamline C_o intersects the line DB (line connecting initial data points) at point S. The properties at point S are obtained by linear interpolation. Three distinct characteristic lines are intersecting at point B1 (*viz.* one streamline and two Mach lines). As shown in table 1, there are two compatibility equations valid along the streamline and one compatibility equation along each Mach line. The flow properties and location at point B1 are obtained by numerically solving the above-mentioned characteristic and compatibility equations from data points B and D, along with that for the streamline passing through point S.

2.1.2. *Points on the curved shock*

The curved shock is obtained by solving discrete points on the shock. Since MoC is not valid across the shock, the solution point at the shock curvature is obtained by iteratively computing the local pressure ratio across the shock. Post-shock properties are calculated with the local incoming Mach number and the assumed pressure ratio across the shock. These flow properties should satisfy the compatibility equation along the C− curve originating from the interior point B1. The iterations stop when this condition is satisfied. The local shock angle is obtained, and the x and y coordinates of the curved shock are obtained by solving the characteristic equations. Subsequent points on the curved shock are obtained by incrementing the next flow turn angle at point D and repeating the above steps. One of the algorithms calculates the interior points in the flow field, while the other determines the discrete points along the shock curvature. Here, ϕ_2 and θ_{eff} represent the shock angle and effective turn angle at the reflection point R, respectively, as shown in figure 3. The analytical model developed does not consider the possibility of Mach reflection and is valid only for regular reflection. The detailed algorithm is described in Appendix A.

2.2. *Moeckel–Chisnell (MC) method*

The MC method consists of finding the shockwave curvature due to the non-uniformities in the flow field. The current approach takes into account a straightforward interaction

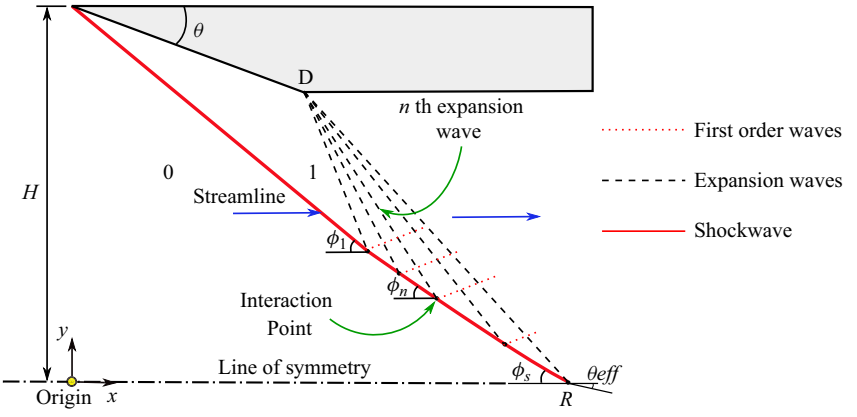

Figure 4. Schematic of shock expansion wave interaction for Moeckel–Chisnell method.

between expansion waves and shockwaves by disregarding any first-order or second-order reflected waves on the flow field. Figure 4 depicts a schematic of the interaction between the expansion fan and shockwave used in the current model. The locations upstream and downstream of the incident shock wave are denoted by 0 and 1, respectively. The expansion fan is partitioned into N waves in the present model, with Mach number and pressure variations following the Prandtl–Meyer relation. The naming convention for the flow field across the expansion waves is identical to that of the incident shockwave, as depicted in figure 4. The interaction point of the *n*th expansion wave with the shock wave is denoted as n, as shown in figure 4.

The flow field downstream of the shockwave in Region 1 is determined by applying the oblique shock relations described in (2.1)–(2.3). The expansion fan turn angle is assumed to be equivalent to the wedge angle.

$$\frac{p_1}{p_0} = \frac{2\gamma}{\gamma+1} M_0^2 \sin^2\phi - \frac{\gamma-1}{\gamma+1}, \tag{2.1}$$

$$\tan\theta = \frac{M_0^2 \sin\phi\cos\phi - \cot\phi}{1 + M_0^2\left(\dfrac{\gamma+1}{2} - \sin^2\phi\right)}, \tag{2.2}$$

$$M_1^2 = \frac{(\gamma+1)^2 M_0^4 \sin^2\phi - 4(M_0^2\sin^2\phi - 1)(\gamma M_0^2 \sin^2\phi + 1)}{[2\gamma M_0^2 \sin^2\phi - (\gamma-1)][(\gamma-1)M_0^2\sin^2\phi + 2]}. \tag{2.3}$$

The incremental Prandtl–Meyer angle ($\Delta\nu$) of any expansion wave is therefore calculated by (2.4). The PM angle is used to compute the pressure and Mach number downstream of the expansion wave as given in (2.5)–(2.8).

$$\Delta\nu = \frac{\theta_w}{N}, \tag{2.4}$$

$$\nu_n = \Delta\nu * n + \nu(M_{n-1}), \tag{2.5}$$

$$\nu_n = \sqrt{\frac{\gamma+1}{\gamma-1}}\tan^{-1}\sqrt{\frac{\gamma-1}{\gamma+1}(M_n^2-1)} - \tan^{-1}\sqrt{M_n^2-1}. \tag{2.6}$$

The pressure (p_n) calculated from the Prandtl–Meyer relation is taken as the pressure at the interaction point of the expansion wave with the shock wave. This pressure is used to

compute the shock wave angle using the oblique shock relation given in (2.9). According to the analysis by Moeckel (1952), the reflection of first-order waves resulting from the interaction between the expansion fan and the shockwave (shown as a dotted red line in figure 4) is negligible and thus disregarded in the model. This method simplifies the computation of the expansion waves downstream of the flow field because it does not interact with any other waves in the flow field.

$$\frac{p_n}{p_{n-1}} = \frac{\left(1 + \dfrac{\gamma - 1}{2} M_{n-1}^2\right)^{\gamma/(\gamma+1)}}{\left(1 + \dfrac{\gamma - 1}{2} M_n^2\right)^{\gamma/(\gamma+1)}}, \tag{2.7}$$

$$\theta_n = \theta_{n-1} - \Delta\nu * n, \tag{2.8}$$

$$\phi_n = \sin^{-1}\left[\frac{1}{M_0}\sqrt{\left[\frac{\gamma + 1}{2\gamma}\left(\frac{p_n}{p_0} - 1\right) + 1\right]}\right]. \tag{2.9}$$

After determining the shock angle, the point of interaction between the shock wave and the expansion wave can be calculated using (2.10)–(2.12). The procedure is executed until the y coordinate becomes zero. This method gives the entire shock curvature with the expansion fan interaction, and works very well, though it has some approximate assumptions as discussed in the sections above. For this reason, the more accurate MoC method is used for constructing the transition lines as explained in the subsequent sections.

$$\frac{Y_{n-1} - Y_n}{X_{n-1} - X_n} = -\tan\phi_n, \tag{2.10}$$

$$\frac{Y_C - Y_n}{X_C - X_n} = \tan(\theta_n + \mu_n), \tag{2.11}$$

$$\mu_n = \sin^{-1}\frac{1}{M_n}. \tag{2.12}$$

3. Shockwave expansion fan interaction – validation with CFD results

For the numerical simulations, a 2-D, inviscid, finite volume, high order shock capturing code is employed. To obtain high-order accuracy and capture the shockwaves without oscillations, the algorithm employs WENO reconstruction. Since the viscous effects are negligible, the inviscid simulations are adequate to explore the shock expansion interaction. The code uses the HLLC approximate Riemann solver for the flux calculation and 4th-order Runge–Kutta ordinary differential equation (ODE) solver to march in time. Further details regarding the numerical method can be found in the literature (Thara Reshma *et al.* 2021; Paramanantham *et al.* 2022). The computational domain is illustrated in figure 5. The inlet of the domain is taken to be 60 mm. We maintain the wedge length at 20 mm. The domain measures 200 mm in length. Figure 5 further displays the boundary conditions used for the present numerical simulations. The domain is discretised with 650×100 cells in the x and y directions, respectively. The validation of the analytical model with CFD is carried out by superimposing the curved shock locus of the more accurate MoC results and the computational results, as shown in figure 6(a). It reveals that the MoC prediction agrees very well with the CFD results qualitatively. The same is done by varying the Mach number, w/H ratio and the wedge angle. The Mach number versus

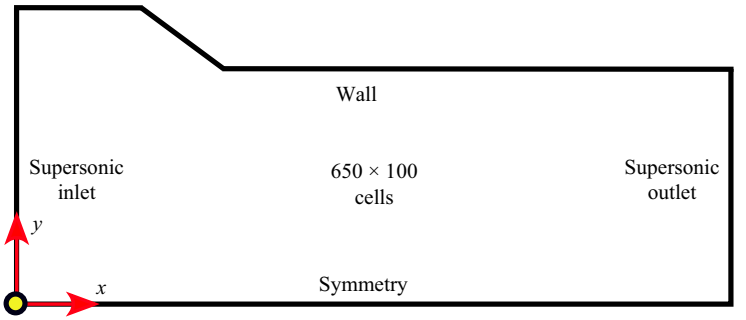

Figure 5. Schematic of computational domain used for the present simulations.

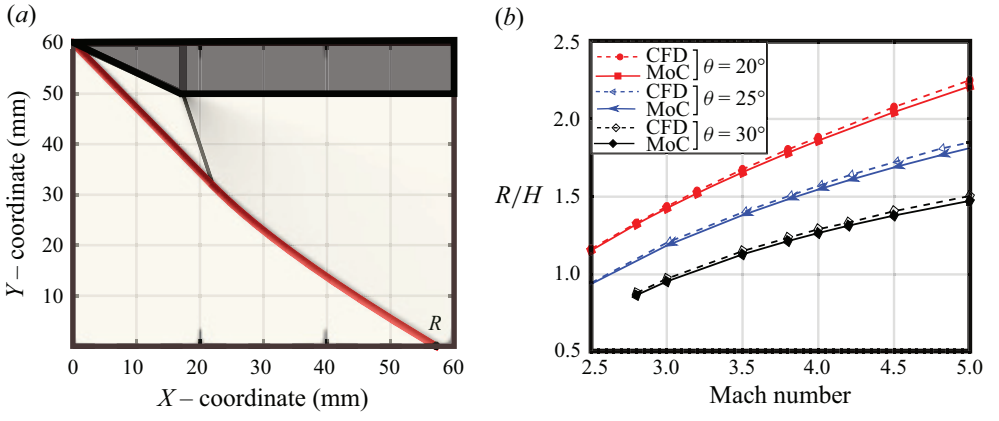

Figure 6. (*a*) Superimposed image of MoC and computational result. (*b*) Validation curve for $w/H = 0.33$ in terms of R/H ratio.

the non-dimensional shock reflection distance (shown in figure 3) (R/H) for different w/H ratios, obtained from analytical and CFD results, are plotted. Figure 6(*b*) shows one such plot of Mach number versus R/H for the w/H ratio 0.33 for different wedge angles. Similarly, the shock angle obtained at the reflection point using the MoC method is compared with that obtained in CFD, as shown in figure 7. It is seen that the maximum difference between the analytical and CFD results is less than 2 %.

4. Shockwave expansion fan interaction – validation with experimental results

4.1. *Supersonic wind tunnel – experimental set-up*

A supersonic wind tunnel is designed and installed to conduct experiments on flow over short wedges. As the investigations are about shock reflections and expansion fan interactions in short wedges, the wind tunnel design should yield a clean flow without strong Mach waves in the test section. The nozzle is a contoured 2-D planar convergent-divergent nozzle with an aspect ratio of 86 mm × 150 mm. The experiments are conducted in such a way as to minimise the edge effects by choosing a bigger aspect ratio wedge and suitable clearance from the side walls to push the shockwave boundary layer interaction downstream (Hornung & Robinson 1982). The test section size has a span of 150 mm to accommodate these requirements. The nozzle contours are designed with the MoC method with boundary layer corrections so as to obtain a uniform flow at

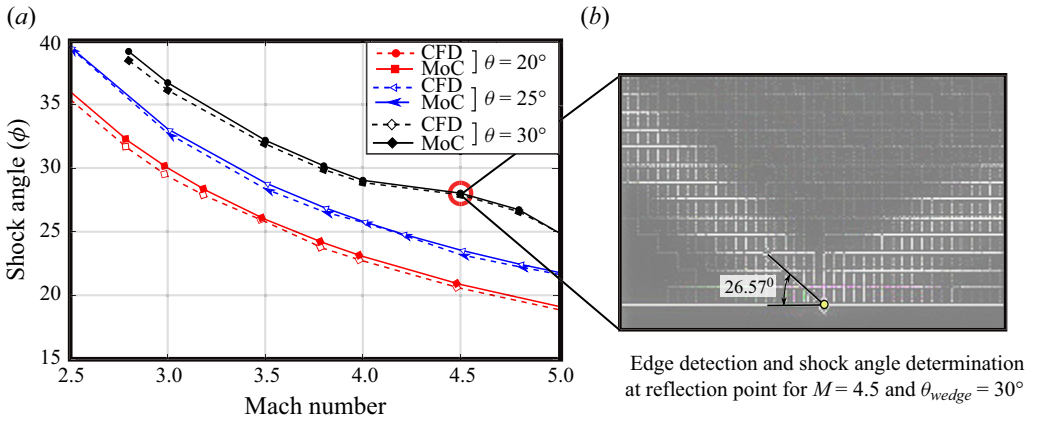

Figure 7. Validation curve for $w/H = 0.33$ in terms of shock angle at reflection point.

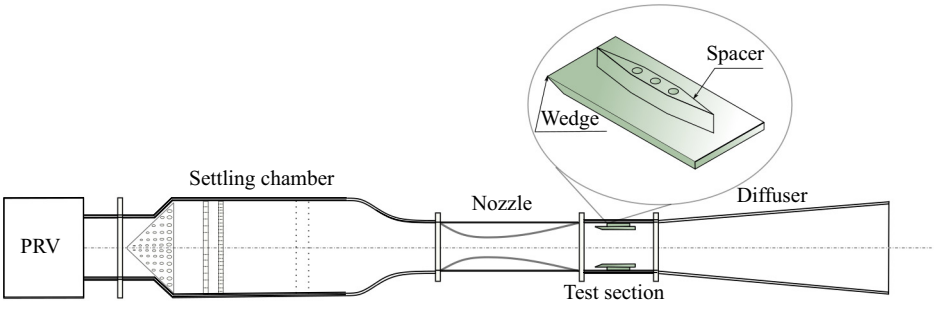

Figure 8. Experimental set-up with wedge.

the test section. The wedges are attached to the top and bottom walls, which have a span of 100 mm and a length of 140 mm. A clearance of 15 mm each from the top and bottom wall is achieved by a spacer of 15 mm thickness, which is machined in the wedge. This spacer, as shown in figure 8, enables the wedge to offset the boundary layer thickness and thus ensures the start of incident shock from the tip of the wedge. Two Mach profiles for the c–d nozzle are manufactured and calibrated to 2.48 and 2.88 Mach numbers.

The stagnation pressure at the settling chamber is controlled by a pressure-regulating valve and the tunnel is started by opening a pneumatically controlled ball valve. The total inlet pressure is measured by a piezo-resistive pressure sensor with a range of 0–20 bar at a sampling rate of 2 kHz. The Z-type shadowgraph imaging is done using an iX CAMERAS i-SPEED 726 at 3000 fps equipped with a Carl Zeiss 100 mm f/2 Makro-planar T* 2/100 lens. The light source is a CAVITAR CAVILUX smart UHS laser with a 30 ns pulse width.

4.2. *Experimental validation of the MoC model developed*

Figure 9(*a–c*) shows the comparison of shadowgraph images with the MoC results by superimposing both images. In figure 9(*a*), the shock curvature which is shown in red colour line is the MoC result and the black colour line indicates the shock captured by the shadowgraph method. The flow properties are $M = 2.48$, $\theta_w = 22.69^\circ$ and $w/H = 0.30$. The pixel size in the shadowgraph image is calibrated with reference to a known dimension in the image. The distance between the tip of the top wedge and bottom wedge (refer to

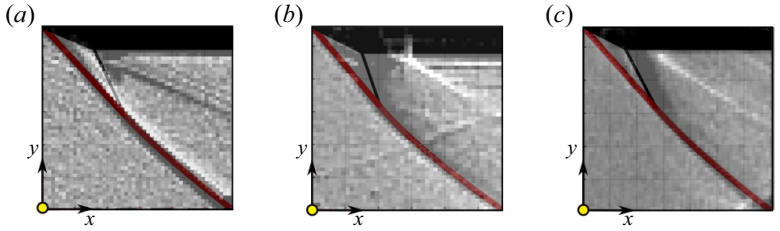

$M = 2.48$, $\theta_w = 22.69°$, $w/H = 0.30$ (short wedge)

$M = 2.88$, $\theta_w = 28.07°$, $w/H = 0.30$ (short wedge)

$M = 2.88$, $\theta_w = 22.69°$, $w/H = 0.30$ (short wedge)

Figure 9. Validation of analytical shock curvature with the experimental shadowgraph image for three short wedges.

M	w/H	θ_w	$\phi_{Analytical}$	$\phi_{Experiment}$	$R/H_{Analytical}$	$R/H_{Experiment}$
2.48	0.3	22.69°	37.27°	$38.66 \pm 0.5°$	1.05	1.12 ± 0.56
2.88	0.3	28.07°	35.50°	$35.54 \pm 0.5°$	1.02	0.958 ± 0.56
2.88	0.3	22.69°	32.08°	$29.74 \pm 0.5°$	1.26	1.312 ± 0.56

Table 2. Analytical (MoC) and experimental results for R/H and the local shock angle at reflection point.

M	θ_w	g	$(R/H)_{Bai}$	$(R/H)_{MC}$	$(R/H)_{MoC}$	ϕ_{Bai}	ϕ_{MC}	ϕ_{MoC}
4.0	25°	0.72	1.2815	1.2840	1.2815	34.1252°	33.8504°	34.1440°
4.0	30°	0.72	1.0448	1.0491	1.0444	36.8219°	36.2464°	36.8965°
4.0	33°	0.76	0.9761	0.9884	0.9741	35.3501°	34.3278°	35.6137°
4.0	35°	0.76	0.8613	0.9101	0.8934	36.7427°	35.1726°	36.7067°
4.5	37°	0.76	0.9	0.9204	0.8947	34.7318°	33.2689°	35.2910°
5.0	40°	0.76	0.8356	0.8645	0.8258	34.4015°	32.5635°	35.3299°

Table 3. R/H value and the local shock angle at the reflection point for three different models.

figure 8) is accurately measured using a Vernier gauge. In the shadowgraph image, this distance was identified and measured in terms of pixels. This procedure was done for three different shadowgraph images (refer to figure 9*a–c*), and one pixel is calibrated to be 0.56 ± 0.02 mm. To find the R/H value, the centre pixel at the reflection point in the image is identified and the horizontal distance from this point to the vertical line drawn through the tip of the wedges is taken in terms of pixels. This distance multiplied by the calibration factor 0.56 ± 0.02 mm will give the distance R, while the distance H is already known. The same is done for all three images and the R/H values are calculated and shown in table 2. Similarly, the approximate shock angle at the reflection point is found using the edge detection technique which uses the 'difference of Gaussians' algorithm and is particularly effective at detecting edges. The R/H value and the local shock angle at the reflection point predicted by the MoC model and that obtained from the shadowgraph images for three different cases are shown in table 2. Table 3 shows a comparison of the R/H values and the shock angle at the reflection point, predicted by three different models (the method of Bai (2023), MC method and MoC method). From table 3, it is evident that the reflection point and the shock angle at the reflection point vary for the three different models as the Mach number and the wedge angle increase.

g	M	$(\theta_w)_{MoC}$	$(\theta_w)_{Bai}$	Percentage error
0.92	2.04	22.02°	23.19°	5.31
0.90	2.21	24.84°	25.91°	4.31
0.88	2.38	27.15°	28.01°	3.18
0.86	2.54	28.11°	29.22°	3.96
0.84	2.74	30.71°	31.72°	3.30
0.80	3.20	34.11°	34.99°	2.58
0.75	3.90	36.67°	37.57°	2.45

Table 4. Maximum error for g lines based on detachment criterion.

5. Results and discussion

The transition of the shock reflection in a short wedge depends on the extent of the interaction of the expansion fan with the incident shock wave. Due to the interaction of the expansion fan, the incident shock is weakened, resulting in a decrease in the shock angle at the reflection point compared with the case where there is no interaction. Therefore, the transition angle between RR and MR is modified. The value of the shock angle at the point of reflection depends on the degree of interaction of the expansion fan, or the w/H ratio, while M and θ remain constant. As stated by Li & Ben-Dor (1997), the transition angle is typically determined using the detachment criterion for RR $\rightarrow$ MR transition or the von Neumann criterion for MR $\rightarrow$ RR transition.

5.1. *Transition lines – comparison with previous studies*

Before discussing the results obtained using the present model, it would be appropriate to compare the results obtained with the previous models developed for the same flow phenomenon (Bai 2023). It is important to know the deviation in obtaining the shock angle and the flow deflection angle at the reflection point using the model of Bai (2023). The model of Bai (2023) uses the parameter g to construct the transition lines. The analytical model developed by Bai (2023) only considers the interaction of C− waves from the trailing edge and does not fully include the effect of reflected C+ waves from the incident shock wave. This approximation would create small errors in prediction of the shock angle at the reflection or triple point since the reflected C+ waves perturb the incoming adjacent C− waves. When the C+ waves are also used to model the flow, as done in this work (MoC method), the slope of the incident shock in the vicinity of the reflection point will be higher when compared with the case where only the C− waves are used (Bai 2023). Therefore, when the flow is modelled using both the C+ and C− waves, the shock angle at the reflection point will be higher when compared with that obtained using the model of Bai (2023) (refer to tables 4 and 5). Hence, this small error affects the prediction of the transition wedge angle at which the RR $\leftrightarrow$ MR transition takes place (i.e. for a given Mach number, the transition happens earlier for the MoC method compared with the model of Bai (2023). This error is evident near to the no-reflection line (red dashed line), as shown in figure 10. The black lines represent the g lines constructed using the method suggested in the work of Bai (2023), whereas the blue lines are those constructed using the present MoC method. The maximum error is calculated by taking the wedge angle corresponding to the intersection point of the g line (black colour) with the no-reflection boundary (red dashed line) and comparing it with that obtained using the MoC method, which is quantified and shown in tables 4 and 5. The point of intersection of the g lines and the no-reflection line is different, as seen in figure 10.

g	M	$(\theta_w)_{MoC}$	$(\theta_w)_{Bai}$	Percentage error
0.90	2.202	24.65°	25.60°	3.85
0.88	2.40	27.41°	28.60°	4.34
0.86	2.64	30.13°	30.93°	2.66
0.84	3	32.62°	33.85°	3.77
0.80	5	38.20°	40.46°	5.90

Table 5. Maximum error for g lines based on von Neumann criterion.

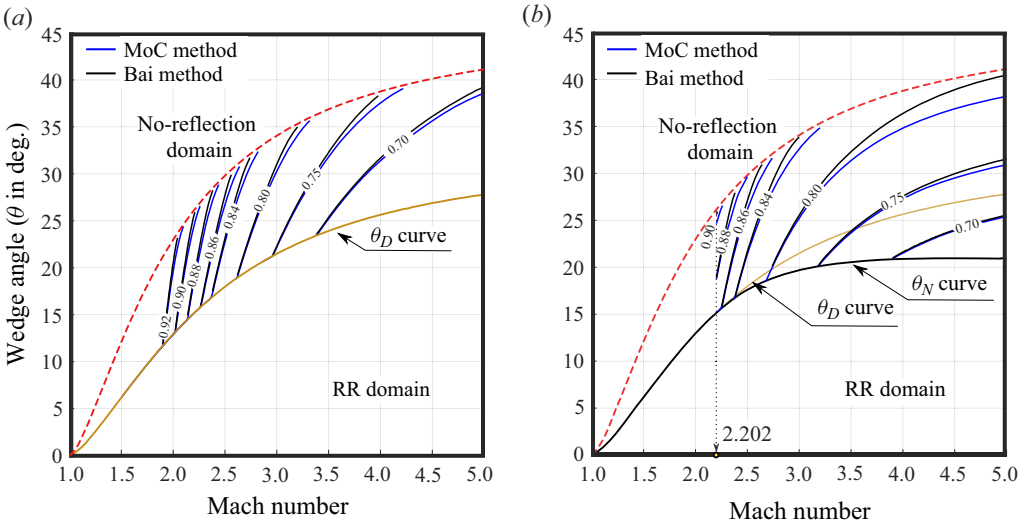

Figure 10. Transition lines for different values of g based on (a) the detachment criterion and (b) von Neumann criterion.

Thus, it is evident that while the modelling approach developed by Bai (2023) matches the MoC method extremely well, there is a small but significant error near the no-reflection boundary. In the following sections, we will quantify the transition angles for the short wedges for various w/H ratios using the MoC method described in § 2 and validate these results with higher-order numerical simulations and shadowgraph images from experiments.

5.2. *Transition lines – detachment criterion validation*

The delay in the transition criterion, or the upwards shift in the detachment criterion line in figure 11(a) for the short wedge, can be attributed to the attenuation of the incident shockwave. The extent of the delay in this transition is determined by the w/H ratio. The determination of the detachment condition involves the solution of MoC for a specified Mach number (M), wedge angle (θ) and w/H. The detachment angle is generally shifted to higher angles for the shorter wedges and ends at the no-reflection domain. The no-reflection domain is the region above the red dashed line. Figure 11(a) shows the shift in the detachment criterion for a w/H ratio of 0.5. The blue line represents the modified detachment criterion resulting from the interaction of the expansion fan with the incident shockwave, whereas the black solid line represents the detachment condition for long

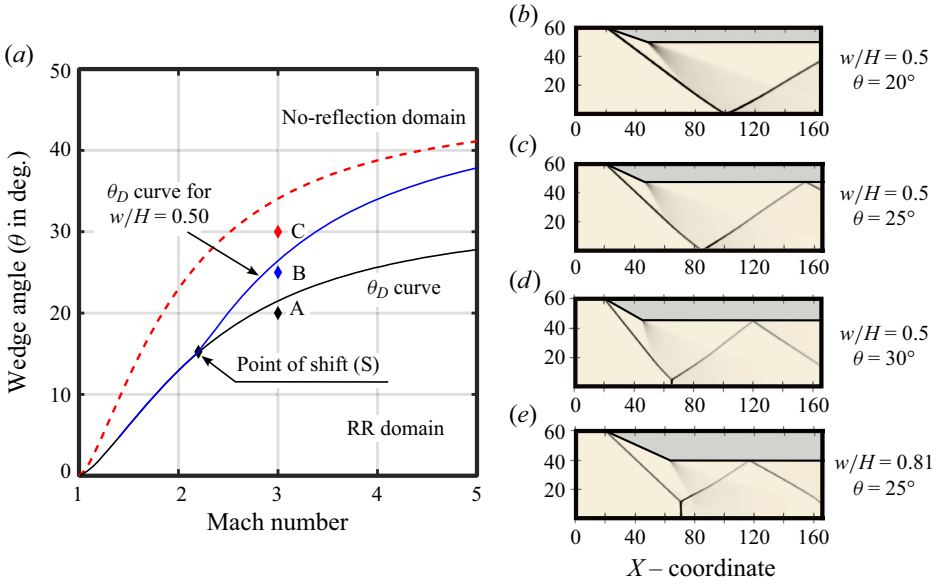

Figure 11. CFD results. (*a*) Transition line – Shift in detachment criterion for $w/H = 0.5$. Flow configurations corresponding to points (*b*) A, (*c*) B, (*d*) C (all short wedges) and (*e*) case without interaction (long wedge), where $M = 3$, $w/H = 0.5$ and $\theta = 20°, 25°, 30°$, respectively, for short wedges, and $M = 3$, $w/H = 0.81$ and $25°$ for the long wedge.

wedges in the absence of expansion fan interaction. Point S in figure 11(*a*) depicts the beginning of the interaction between the expansion fan and the incident shock wave for a given w/H ratio. The deviation of the detachment condition occurs after this value, and for values below the interaction point (S), it remains the same as the long wedge. The point of shift (S) always depends on the extent of interaction and thus depends on the w/H ratio. Interesting observations in the point of shift (S) for various w/H ratios will be examined towards the end of this section. The transition line obtained from the MoC is validated with numerical simulations for $M = 3$ flow over a supersonic wedge; three cases are considered by keeping the Mach number constant and varying the wedge angle to comprehend the type of reflection obtained from the numerical simulations. The wedge angles are set to $\theta_w = 20°, 25°, 30°$, respectively (points A, B and C in figure 11*a*), and w/H is set to 0.5 (short wedge case) and 0.81 (long wedge case). Figure 11(*b–e*) depict the numerical Schlieren of the short wedge flow fields at points A, B and C, and the long wedge flow field simulation at point B. It can be seen from figure 11(*b–e*) that the shock reflections corresponding to points A and B are regular reflections, and C is the Mach reflection for the short wedge, while for point B, it is a Mach reflection for the long wedge. This confirms the shift of the transition line for a short wedge, making a regular reflection at point B, which was an erstwhile Mach reflection for the long wedge.

The experimental validation of the shift in the transition line from the θ_D curve is validated from the shadowgraph images from the experiments. Experiments were done for flow variables corresponding to P, Q and R as shown in figure 12(*a*), where the w/H ratio is 0.30. At points P and Q, the flow variables are $M = 2.48$, and wedge angles are $\theta = 28.07°$ and $22.69°$, respectively. Point P is just above the blue colour transition line ($w/H = 0.30$), as seen in figure 12(*a*), which results in an MR flow configuration as verified by the shadowgraph image in figure 12(*b*) from the experiment. Point Q is below the transition line, which results in an RR, as verified by the image in figure 12(*c*).

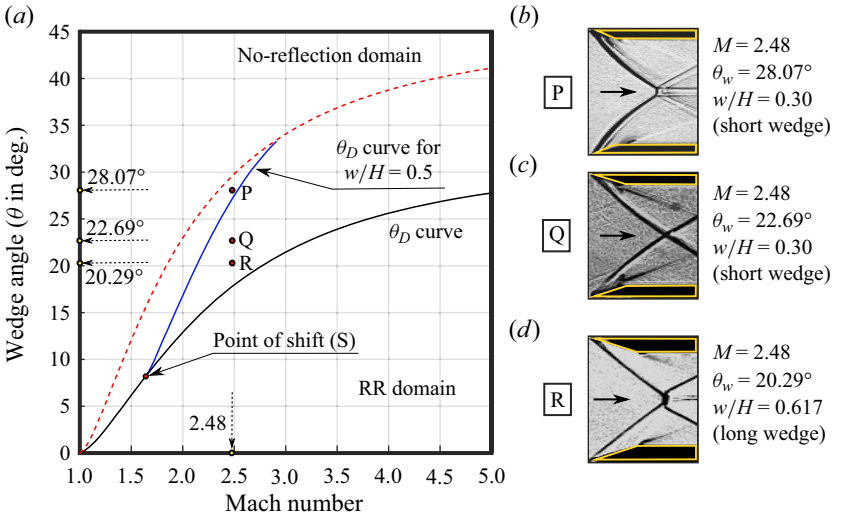

Figure 12. Experimental results. (*a*) Transition line – Shift in detachment criteria for $w/H = 0.30$. Flow configurations corresponding to points (*b*) P, (*c*) Q (both short wedges) and (*d*) R (long wedge); where $M = 2.48$, $w/H = 0.30$ and $\theta = 28.07°, 22.69°$, respectively, for short wedges, and $M = 2.48$, $w/H = 0.617$ and $20.29°$ for the long wedge.

At point R, the w/H ratio is 0.617 (long wedge), where $M = 2.48$ and $\theta = 20.29°$. This is above the θ_D curve (black colour), which should give an MR as validated by the image in figure 12(*d*). It is worth mentioning that the shock configuration is an MR for a long wedge (point R) and an RR for a short wedge (point Q). This confirms that the transition line has shifted to higher wedge angles when we use a short wedge. Thus, from the experiment results, it is clear that the transition line drawn for $w/H = 0.3$ predicts the RR $\rightarrow$ MR transition correctly. The slight asymmetry seen in the Mach stem in figure 12(*b*) is due to the small offset in the leading edge of the bottom wedge when compared with the top wedge (+0.3 mm), whereas that in figure 12(*d*) is due to a small error in the wedge angle ($\pm 0.2°$).

Similarly, experiments are done for Mach number 2.88 and w/H ratio 0.52, as shown in figure 13. At points S and T, the flow variables are $M = 2.88$, and wedge angles are $\theta = 28.07°$ and $22.69°$, respectively. Similar to the previous experiment, point S is just above the blue colour transition line (w/H =0.52) and point T is below the transition line, as seen in figure 13(*a*). Point S corresponds to an MR flow configuration as verified by the shadowgraph image in figure 13(*b*) from the experiment. Point T is below the transition line, which results in an RR, as verified by the image in figure 13(*c*).

Figure 14 demonstrates that for all w/H ratios, a combination of M–θ_w exists for which the interaction begins, and the transition line shifts from that point. Figure 14 shows that $w/H = 0.33$ begins to deviate from the detachment condition line at point S, where $M = 1.74$ and $\theta_w = 9.6°$. The shift ends at the no-reflection condition at point E corresponding to $M = 3.38$ and $\theta_w = 36.3°$. For $w/H = 0.33$, the region under the curve SEPD will be a combination of pure RR and dual solution domain, which eliminates pure MR flow configurations for any combination of Mach number and wedge angle in the region. If a w/H ratio as small as 0.05 is used for the wedge, it can be seen from the figure 14 that we can even eliminate the pure Mach reflection completely and ensure that the entire M–θ_w plane will have regular reflection. Thus, the development of transition conditions for a shorter wedge has far-reaching implications that one can select a domain in which

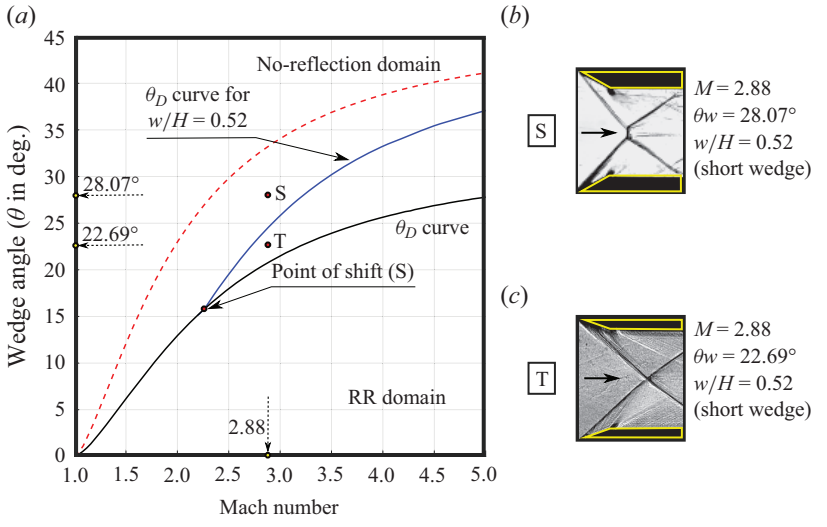

Figure 13. Experimental results. (*a*) Transition line – Shift in detachment criteria for $w/H = 0.52$. Flow configurations corresponding to points (*b*) S and (*c*) T (both short wedges); where $M = 2.88$, $w/H = 0.52$ and $\theta = 28.07°, 22.69°$, for points S and T, respectively.

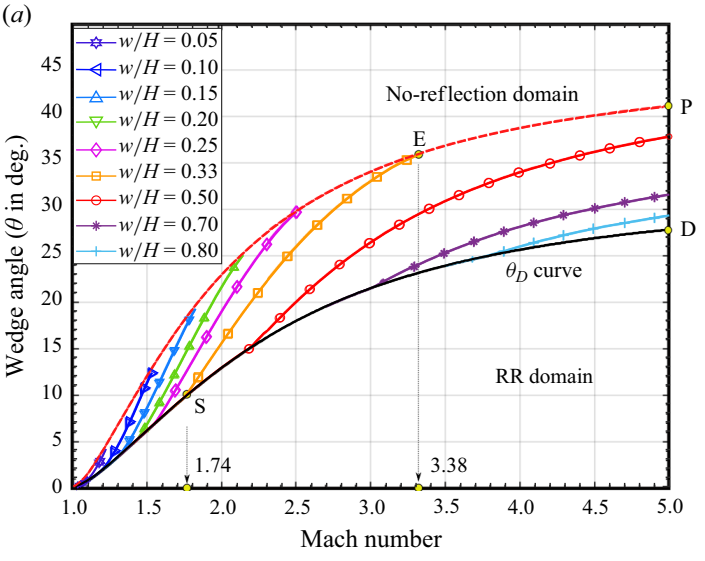

Figure 14. Transition line – Shift in detachment criterion for different w/H ratios.

only a regular reflection occurs or control the size of the Mach reflection configuration by adjusting the w/H ratio.

From figure 14, it can be observed that for values of w/H ratio typically greater than 0.50, the point of shift (S) occurs at Mach numbers greater than 2, and for w/H values less than 0.5, the point of shift (S) occurs at Mach numbers close to or less than 2. In fact, from the oblique shock relations, it is evident that for Mach numbers less than 2, the shock angle is comparatively more than that with Mach numbers greater than 2 for the same wedge angle. Thus, for Mach numbers less than 2, the point of intersection of the incident

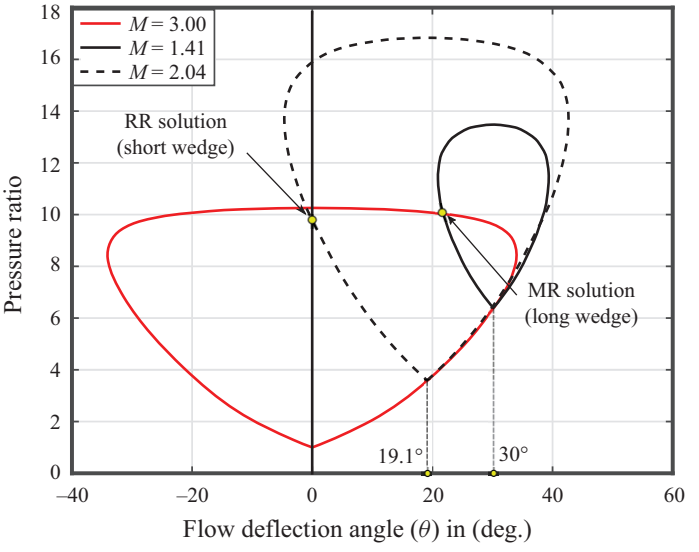

Figure 15. Shock polar representation for $w/H = 0.33$.

shock and the first expansion wave from the trailing edge (point B in figure 3), will occur only at very small wedge length (w). Thus, in the case of bigger values of wedge length or larger w/H ratios, and for flow Mach numbers say less than 2, the incident shock angle will meet the symmetry line before the first expansion wave intersects the incident shock. This flow characteristic is the same as that occurs in a long wedge. Thus, the transition line will remain the same as that for a long wedge unless the intersection occurs which leads to shock angle reduction due to interaction effects.

Figure 15 depicts the polar shock representation of a long and short wedge with a w/H ratio of 0.33. The incoming flow has a Mach number of 3 and a wedge angle of 30°. The post-shock Mach number at the reflection point for a long wedge is 1.41, while that for a short wedge is 2.04. The post-shock Mach number at the reflection point for a short wedge is higher due to the effective shock angle reduction at the reflection point due to the trailing edge expansion fan interaction. The shock polar also reveals that in the short wedge, due to the expansion fan interaction, there is a decrease in the required flow turn angle (19.1°) at the reflection point, even though the wedge angle (30°) remains unchanged. For a long wedge, the θ_{max} for the post-shock Mach number of 1.41 is 9.62°, whereas for the short wedge mentioned above, the post-shock Mach number is 2.04 and the θ_{max} is 23.65°.

Thus, at the reflection point, the required flow turn angle for a short wedge is 19.1°, which is less than the θ_{max} value of 23.65°. This results in a regular reflection. The shock polar yields the MR solution corresponding to the long wedge and the RR solution corresponding to the short wedge.

5.3. *Dual solution domain in short wedges*

Another significant transition criterion in the wedge flows is the von Neumann criterion. Intuitively, it makes sense to assume that as the w/H ratio decreases, the von Neumann criterion line also shifts towards higher wedge angles, similar to the detachment condition. The dual solution domain, which is the region between the detachment criterion line and the von Neumann criterion line, also undergoes this shift. To comprehend the change in the dual solution domain, transition lines for the von Neumann criterion were also drawn for

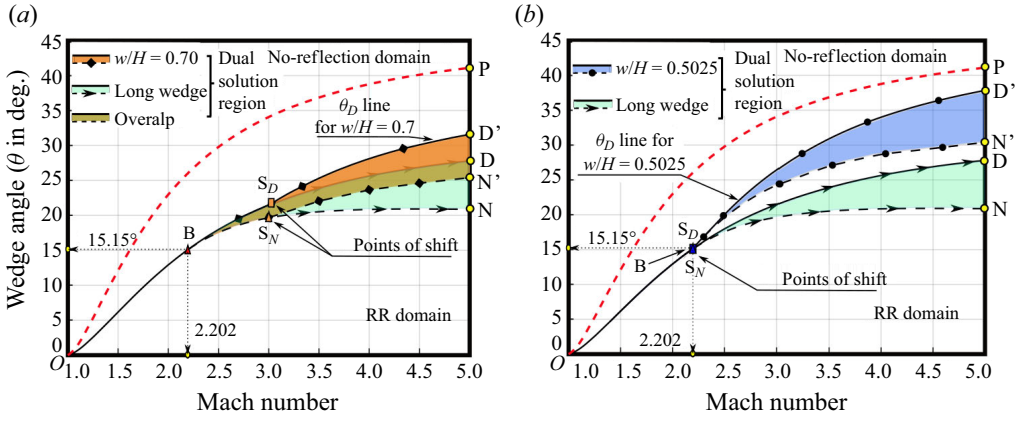

Figure 16. Dual solution domains for short wedges and long wedges (refer to the legend). (*a*) $w/H = 0.7$ shown in orange colour and long wedge shown in green colour; (*b*) $w/H = 0.5025$ shown in blue colour and long wedge shown in green colour.

various w/H ratios. The von Neumann criterion line for the short wedge is more complex than the detachment criterion, owing to the existence of the weak Mach reflection domain below Mach numbers 2.202 for air, which is marked as point B (bifurcation point) in figure 16(*a*). The shifts in the dual solution domain are divided into three categories as: Type I dual solution domain, in which the shift due to interaction occurs after the von Neumann point; Type II dual solution domain, where the detachment criterion line shift occurs before the von Neumann point; and Type III dual solution domain, where the von Neumann point itself has shifted due to high interaction and intersects the no-reflection line resulting in no dual solution domain. These peculiar flow phenomena are discussed in detail in the forthcoming sections below.

5.3.1. *Type I dual solution domain*

In the type I domain, the von Neumann point 'B' is identical to the long wedge flows, and the von Neumann criterion follows the long wedge path prior to expansion fan interaction and then shifts to higher wedge angles once the expansion fan interaction commences. The region above the red dashed line indicates a no-reflection domain where the shock waves are not attached to the wedge. To explain the shift in the dual solution domain, the whole dual solution region (region between the von Neumann criterion transition line and the detachment criterion transition line) is colour coded and shown in the legend of the figures for quick reference. For instance, in figure 16(*a*,*b*), the green colour region indicates the dual solution domain for long wedges (wedge with no expansion fan interaction with the incident shock). The dual solution domain region for w/H ratio 0.7 is shown as orange colour in figure 16(*a*). Note that this region overlaps the dual solution region for the long wedge (i.e. the orange colour overlaps the green colour). All these regions can be quickly identified from the legend of figure 16(*a*). Similarly, the dual solution region for w/H ratio 0.5025 is shown as blue colour in figure 16(*b*) and the dual solution domain for long wedge is shown as green colour. The nature of the shift is explained as follows.

The von Neumann criterion (θ_N) line and detachment criterion (θ_D) line for w/H ratio 0.7 is shown in figure 16(*a*). The paths OBS$_D$D and OBS$_N$N represent the θ_D and θ_N lines for long wedges. Both the transition lines follow the same path as that for a long wedge, up to the points of shift (S$_D$ and S$_N$ for the detachment line and von Neumann line,

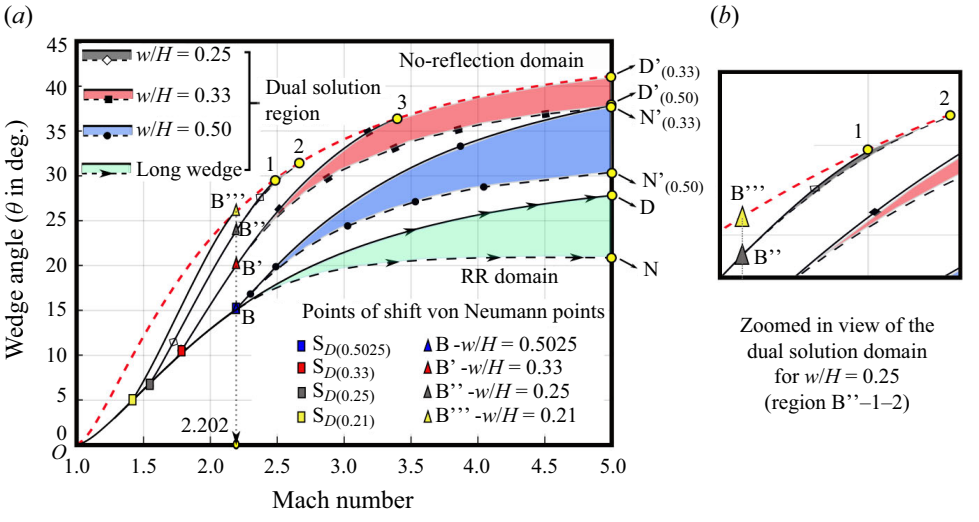

Figure 17. Dual solution domains for long and short wedges.

respectively), then follow a different path as (S_D–D' and S_N–N') for a short wedge. The paths OBS$_D$D' and OBS$_N$N' represent the θ_D and θ_N line for a short wedge. The point of the shift of the θ_D line is at point S$_D$, where $M = 3.03$ and wedge angle $\theta_W = 21.66^\circ$, whereas the point of the shift of the θ_N line is at point S$_N$, where $M = 3$ and wedge angle $\theta_W = 19.66^\circ$. As the w/H value decreases from 0.7, the point of shifts S$_D$ and S$_N$ moves to the direction of the von Neumann point B, and merges with the point B, where $M = 2.202$, $\theta_W = 15.15^\circ$ and the w/H ratio is 0.5025, as shown in figure 16(b). Thus, short wedges with w/H ratios greater than 0.5025 will give a Type I dual solution domain. The characteristic of this type is that the weak Mach reflection or von Neumann point B remains the same for all w/H ratios greater than 0.5025 since both the points of shift from the detachment line and von Neumann line S$_D$ and S$_N$ occur after point B.

5.3.2. *Type II dual solution domain*

As illustrated in figure 17, the type II dual solution domain occurs when the detachment condition occurs prior to the von Neumann point B for w/H ratios less than 0.5025. Consequently, the type II domain begins at $w/H = 0.5025$ and ends at $w/H = 0.21$, where the von Neumann point (B) reaches the no-reflection line (point B''' in figure 17). The dual solution domains for w/H ratios 0.25, 0.33, 0.5025, and long wedge are shown in figure 17. In the figure, for the long wedges, paths OBD and OBN represent the θ_D and θ_N lines, respectively. The dual solution region for the long wedge is colour coded as green. Path OBD'$_{(0.5)}$, OBN'$_{(0.5)}$, represents the same for short wedge of w/H ratio 0.5025. The dual solution region for the short wedge with a w/H ratio of 0.5025 is colour coded as blue. This ratio corresponds to the start of the Type II dual solution domain. The dual solution regions for different w/H ratios can be easily identified by referring to the legend in figure 17.

For short wedge with w/H ratio 0.33, the θ_D line and θ_N line follow the path OB'D'$_{(0.33)}$ and OB'N'$_{(0.33)}$, respectively, as shown in figure 17. The dual solution region for this short wedge with w/H ratio of 0.33 is colour coded as red. The dual solution region for this case is quite interesting. The detachment criterion line intersects the no-reflection line at point 3 and then follows the no-reflection line boundary (red dashed line) and ends at D'$_{(0.33)}$.

A major part of the dual solution domain is between the no reflection line boundary and the $\theta_{N'0.33}$ line. Thus, in this case where the w/H ratio is 0.33, the pure Mach reflection is confined to a very small region in the M–θ_w plane, which is in between the no-reflection line (red dashed line) and the curve O-$S_{D(0.33)}$-3. In § 5.2 (refer figure 14), it has been seen that pure Mach reflections can be completely turned into regular reflections for very small w/H ratios. In the following discussion, we will find out a w/H ratio to completely avoid the dual solution domains.

The θ_D line and θ_N line for w/H ratio 0.25 are shown as path OB"1 and OB"2, respectively. The dual solution domain for $w/H = 0.25$ is extremely small, as seen in the zoomed-in picture in figure 17. The dual solution domain is hardly visible for wedges with w/H ratios less than 0.25. Thus, for short wedges with w/H ratios less than 0.5025, the von Neumann point B shifts in the direction of the no-reflection domain and eventually meets the no-reflection line at point B"', where the θ_D line of w/H ratio 0.21 intersects with the no-reflection line. Moreover, the characteristic nature of Type II dual solution domains is that, as the w/H value is reduced from 0.5025 to 0.21, the dual solution domain diminishes and shifts towards the no-reflection domain.

5.3.3. *Type III dual solution domain*

The von Neumann solution does not exist for long wedges for Mach numbers less than 2.202, where the wedge angle $\theta_w = 15.15^\circ$. However, in short wedges, as the w/H ratio decreases, the wedge angle corresponding to the von Neumann point moves to higher wedge angles. The limiting case of this shift in wedge angle is when the von Neumann point intercepts the no-reflection line shown as point B"' in figure 17. The value of the w/H ratio whose θ_D line passes exactly through this point B"' will give the limiting point of von Neumann solutions in short wedges. The value calculated is very close to 0.21, neglecting the numerical errors. The θ_D line for w/H ratio 0.21 is shown in figure 17 as path OB"', in which point $S_{D(0.21)}$ is the point of the shift from the θ_D line, where $M = 1.44$ and $\theta = 5.3^\circ$. The von Neumann point is at point B"', where $M = 2.202$ and wedge angle $\theta = 25.93^\circ$. Thus, the M–θ_w parameter space where the value of w/H is less than 0.21 characterises the type III domain. Type III domain differentiates itself from the other two domains as no dual solution domain exists in this type, and only pure MR and pure RR exist. However, the region for pure MR is confined to a very small space in the M–θ_w plane.

5.3.4. *Locus of the von Neumann points*

Shifting the von Neumann point is one of the defining characteristics of the short wedge flows. It is evident from the preceding discussion that for w/H ratios less than 0.5025, the von Neumann point moves, and figure 18 illustrates the locus of shift of the von Neumann points in the red dashed line (the line connecting points $S_{D(0.5025)}$ and $B_{0.21}$ in figure 18) for various w/H ratios. This demarcation line divides the M–θ_w space into two distinct areas. Dual-domain solutions do not exist on the left-hand side of the line, but exist on the right. The shift in von Neumann points in the M–θ_w parameter space follows a straight line passing through the x-intercept where $M = 2.202$. Although the dual solution domain exists on the right-hand side of the above-mentioned straight line, the domain close to this line is hardly visible due to the interaction effects, as shown in the enlarged views of regions B1 and B2 in figure 18. To confirm the shift in von Neumann point B, shock polars of short wedges with actual wedge angle and effective wedge angle (turn angle at reflection point) are drawn. Figure 19 shows the shock polar for w/H ratio 0.33 at the

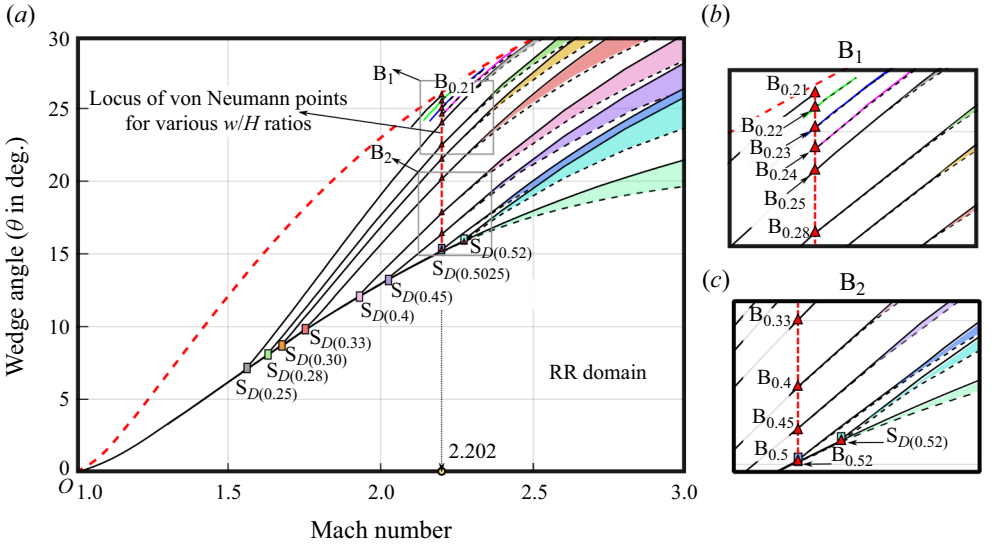

Figure 18. Locus of bifurcation points for various w/H ratios.

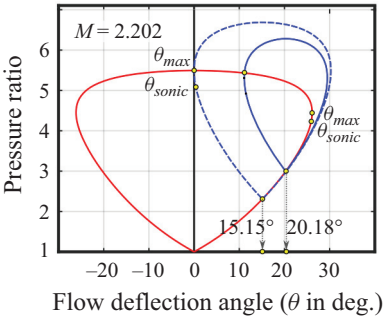

Figure 19. Shock polar for $M = 2.202$, w/H ratio 0.33.

von Neumann point $B_{0.33}$ (refer to region B2 in figure 18). The solid blue line indicates r-polar for the actual wedge angle used, and the dashed blue line shows the same for the effective wedge angle θ_{eff} at the reflection point R (refer to figure 3). At point $B_{0.33}$, the wedge angle is 20.18° and due to interaction, this is reduced to 15.15°. Thus, the von Neumann shift in short wedge flows is validated with the shock polar. Further investigations are required to comprehend the shock reflection configurations and the flow behaviour in Type I, Type II and Type III interactions in the flow over short wedges.

6. Conclusion

The shock reflection phenomena on short wedges have been investigated using analytical, computational and experimental methods. The interaction of the expansion fan emanating from the trailing edge of the short wedge with the incident shock wave is found to curve the incident shock. The curving of the incident shock wave leads to the change of shock angle at the reflection/triple point, consequently leading to a shift in the transition line. The transition lines plotted for different w/H ratios from 0.05 to 0.8 show that the shift in transition lines depends on the extent of interaction. The plot is useful in finding the

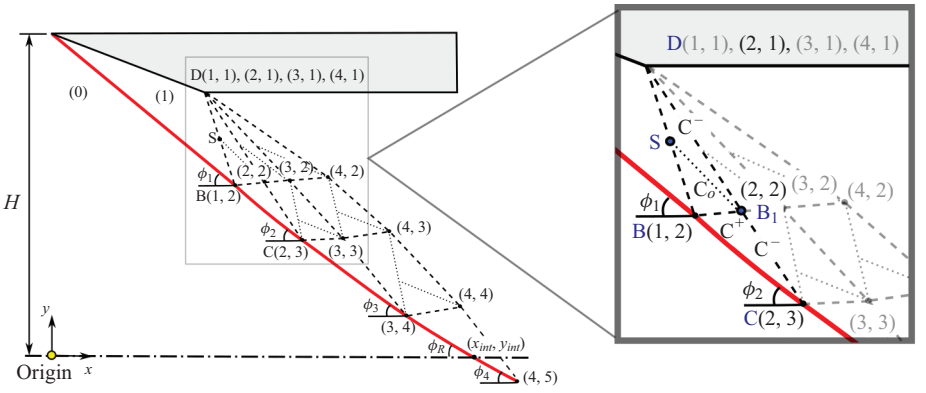

Figure 20. Framework for solution algorithm in MoC.

detachment/von Neumann criterion for any Mach number between 1 and 5 for a particular w/H ratio. Moreover, we can control the appearance of MR or its configuration for a particular Mach number by selecting the suitable (w/H) ratio from the transition lines generated. As the extent of expansion fan interaction with the incident shock increases, the dual domain shifts its location. Based on the pattern of shift the dual solution regimes are classified into Type I, Type II and Type III domains. The dual solution domain eventually diminishes as a function of w/H ratio, facilitating the control of the MR $\leftrightarrow$ RR hysteresis process.

Declaration of interests. The authors report no conflict of interest.

Author ORCIDs.
Vinod Yeldho Baby https://orcid.org/0009-0009-8726-0430;
Vinoth Paramanantham https://orcid.org/0000-0003-3445-5460;
G. Rajesh https://orcid.org/0000-0002-4459-7676.

Appendix A. Analytical modelling

This section explains in detail the algorithm developed and governing equations used to find the curvature of the incident shock due to the interaction of the trailing edge expansion waves of the same family. The reference book for developing the algorithm is Zucrow & Hoffmann (1977).

The present study assumes steady, two-dimensional planar flow of a perfect gas which is rotational in nature. Two algorithms are developed, one to find the interior points in the flow field and the other to find the discrete points on the shock. The incoming flow is assumed to be horizontal. After the initial deflection of the flow at leading edge of the wedge, the flow near the trailing edge turns back to horizontal direction due to the expansion fans from the trailing edge. To achieve this, the shoulder of the wedge is made parallel to the line of symmetry. The coordinate system used in the solving algorithm and the framework of number system to denote the position in the flow field is as shown in figure 20.

The input to the code is Mach number (M_0), wedge angle (θ_w) and w/H ratio. The stagnation pressure (P_0) and temperature (T_0) are assumed to find the flow property values. With this input, the x,y coordinates of the trailing edge, point D (1, 1), as shown in figure 20, are calculated. The first expansion line is drawn from point D after finding the Mach angle as $\mu = \arcsin(1/M_1)$, where M_1 is the Mach number post shock. This will intersect the incident shock at B (1, 2) as shown in figure 20. The flow property values of

pressure (p), density (ρ), velocity (V), flow turn angle (θ) are calculated at point B using the oblique shock relations.

To begin the algorithm, a small turn angle dθ is assumed to happen at the trailing edge (point D). For this flow turn angle, the flow property values are calculated at point D (2, 1) from the Prandtl–Meyer relations and isentropic relations shown in (A1)–(A2). Note that at point D, although the (x, y) location remains the same, the flow property value changes depending on the turn angle in each step. Now the initial data points are D (2, 1) and B (1, 2). With these points, the next interior point B_1 (2, 2) is calculated as follows:

$$\nu_i = \sqrt{\frac{\gamma+1}{\gamma-1}}\tan^{-1}\sqrt{\frac{\gamma-1}{\gamma+1}(M_i^2-1)} - \tan^{-1}\sqrt{M_i^2-1}, \tag{A1}$$

$$\frac{p_i}{p_{01}} = \left(1+\frac{\gamma-1}{2}M_i^2\right)^{(\gamma-1)/\gamma}, \tag{A2}$$

where

$$i = 1, 2, 3, \ldots \quad \text{at point } D. \tag{A3}$$

From the characteristic equations given in table 1, the following four ((A4)–(A7)) are written in the finite difference form. These equations are simultaneously solved for obtaining values x_S, y_S, x_{B1} and y_{B1}. The properties such as V, θ, p and ρ at point S are obtained by linear interpolation (line DB). Note that as shown in (A11) and (A12), the value of θ_S is computed by the iterative method. For each iteration, the value of θ_S is linearly interpolated and substituted in (A4), and the value of x_S is computed till the difference from this value and the previous value is minuscule.

$$\frac{(y_S - x_S)}{(y_{B1} - x_{B1})} = \lambda_0, \tag{A4}$$

$$\frac{(y_{B1} - x_{B1})}{(y_D - x_D)} = \lambda_+, \tag{A5}$$

$$\frac{((y_{B1} - x_{B1})}{(y_B - x_B)} = \lambda_-, \tag{A6}$$

$$\frac{(y_S - x_S)}{(y_B - x_B)} = \lambda_{DB} \quad \text{(slope of line DB)}, \tag{A7}$$

where

$$\lambda_+ = \tan(\theta + \mu), \tag{A8}$$

$$\lambda_- = \tan(\theta - \mu), \tag{A9}$$

$$\lambda_0 = \tan(\theta_S), \tag{A10}$$

$$\text{where} \quad \theta_S = \frac{(\theta_D + \theta_B)}{2} \quad \text{(first guess)}, \tag{A11}$$

$$\text{and} \quad \theta_S = \frac{(\theta_S + \theta_{B1})}{2} \quad \text{(next iteration)}. \tag{A12}$$

The compatibility equations along the C− and C+ lines can be written in the finite difference form as

$$Q_+(p_{B1} - p_B) + (\theta_{B1} - \theta_B) = 0, \tag{A13}$$

$$Q_-(p_{B1} - p_D) - (\theta_{B1} - \theta_D) = 0, \tag{A14}$$

where

$$Q_+ = \frac{\sqrt{M_B^2 - 1}}{\rho_B V_B^2} \quad \text{and} \quad Q_- = \frac{\sqrt{M_D^2 - 1}}{\rho_D V_D^2}. \tag{A15}$$

The compatibility equations along the stream line C_0 can be written in the finite difference form as

$$R_0(V_{B1} - V_S) + (p_{B1} - p_S) = 0, \tag{A16}$$

$$(p_{B1} - p_S) - A_0(\rho_{B1} - \rho_S) = 0, \tag{A17}$$

where

$$R_0 = \rho_S V_S \quad \text{and} \quad A_0 = a^2 = \frac{\gamma p_S}{\rho_S}. \tag{A18}$$

Equations (A13)–(A17) can be solved to get values p, θ, ρ and V, at point B_1. The values found till now, including the location of B_1 (2, 2) and the flow property values V, θ, p and ρ at that location, form the predictor values of an Euler predictor algorithm. Improved values (corrector) for the location B_1 (2, 2) and the corresponding flow property values V, θ, p and ρ at that location may be obtained by repeating the steps discussed above for the Euler predictor algorithm by using average values of V, θ, p and ρ along each characteristic line. For instance, for C+ characteristic line, the values may be recalculated by taking the average as

$$\lambda_+ = \tan(\theta_+ + \mu_+), \tag{A19}$$

where

$$p_+ = \frac{(p_B + p_{B1})}{2}, \quad \theta_+ = \frac{(\theta_B + \theta_{B1})}{2}, \quad V_+ = \frac{(V_B + V_{B1})}{2}, \quad \rho_+ = \frac{(\rho_B + \rho_{B1})}{2}. \tag{A20}$$

Additionally, sound velocity, Mach number and Mach angle can be averaged as

$$a_+ = \sqrt{\frac{\gamma p_+}{\rho_+}}, \quad M_+ = \frac{V_+}{a_+}, \quad \mu_+ = a \sin \frac{1}{M_+}. \tag{A21}$$

Thus, the modified Q_+ can be calculated as

$$Q_+ = \frac{\sqrt{M_+^2 - 1}}{\rho_+ V_+^2}. \tag{A22}$$

The coefficients $\lambda_-, \lambda_0, Q_-, R_0$ and A_0 are determined in a similar manner. The corrector can be iterated to achieve the required accuracy level. The above steps are repeated till the required convergence is met. This completes the interior point calculation algorithm.

The next point in the framework is C (2, 3), which is a point on the curved shock. Since the MoC equations are not valid across the shock, oblique shock relations are used across the shock, and the characteristic and compatibility equations are used post shock to solve this point. At this point C (2, 3), the shock angle has reduced from ϕ_1 to ϕ_2 due to the expansion wave interaction as shown in figure 20. The subsequent part of this algorithm is developed to find out the modified shock angle and the flow properties post shock at point C. This is obtained by an iterative method which is explained as follows.

First, a pressure ratio across the shock at that vicinity is assumed. The best guess is the pressure at point B (1, 2). In fact, in the MC approach, this pressure is taken as

M	wedge angle (θ_w)	w/H	step size (dθ)	R/H	ϕ_R
2.5	20°	0.33	0.1°	1.154	36.02°
2.5	20°	0.33	0.05°	1.154	36.02°
2.5	20°	0.33	0.03°	1.154	36.01°
2.5	20°	0.33	0.01°	1.154	36.01°
2.5	20°	0.33	0.005°	1.154	36.01°
3	30°	0.33	0.1°	0.9546	36.74°
3	30°	0.33	0.05°	0.9546	36.74°
3	30°	0.33	0.03°	0.9547	36.71°
3	30°	0.33	0.01°	0.9547	36.71°
3	30°	0.33	0.005°	0.9547	36.71°

Table 6. MoC results to find the convergence in step size (dθ).

the post-shock pressure and the shock angle is calculated accordingly. Here, we use the pressure at B (1, 2) to find the pressure ratio across the shock as (p_B/p_∞) and use that value as the first guess. With the incoming Mach number (M_∞) and assumed pressure ratio (p_B/p_∞), the shock angle (ϕ_2) and the flow turn angle θ_C at point C (2, 3) is calculated. For the C− characteristic line from B_1 (2, 2) to C (2, 3), the compatibility equation given in table 1 is written in the finite difference form as

$$Q_-(p_{B1} - p_C) - (\theta_{B1} - \theta_C) = 0, \tag{A23}$$

where

$$Q_- = \frac{\sqrt{M_{B1}^2 - 1}}{\rho_{B1} V_{B1}^2}. \tag{A24}$$

The θ_C value calculated at point C from the first guess is then incorporated into (A23) and the pressure (p_C) at C is calculated. This pressure should match with the post-shock pressure calculated from the guess. The procedure is repeated till the required convergence is met. Its worth mentioning that the C− characteristic line starting from point D, which ends at the curved shock, is slightly modified by the C+ lines which are generated from the incident curved shock. To find the next local shock angle ϕ_3, the next characteristic line is generated for the next increment in flow turn angle (dθ) at the point indicated as D (3, 1) as shown in figure 20. The flow property values V, θ, p, M and ρ at locations (3, 1), (3, 2), (3, 3) and (3, 4) are calculated and the local shock angle (ϕ_3) at location (3, 4) is obtained using the algorithm mentioned above. To construct the curvature of the shock, the adjacent shock angles are averaged. The algorithm is executed till the flow at point D has become horizontal, or the curved shock hits the line of symmetry. The exact point of intersection of the curved shock with the line of symmetry, (x_{int},y_{int}) as shown in figure 20, is obtained by a linear interpolation between the points (3, 4) and (4, 5). The shock angle (ϕ_R), flow turn angle (θ_{eff}) and all the flow properties at this intersection point are obtained by linear interpolation.

The minimum step size (dθ in degrees) required for the accurate prediction of the curvature of the incident shock is found out by reducing the value of (dθ) from 0.1° to 0.005° and computing the corresponding R/H values and shock angle ϕ_R at the reflection point for each case. The results for two cases are shown in table 6 and the optimum step size (dθ) for executing the algorithm is taken as 0.03°.

References

Azevedo, D.J. & Liu, C.S. 1993 Engineering approach to the prediction of shock patterns in bounded high-speed flows. *AIAA J.* **31** (1), 83–90.

Bai, C.-Y. 2023 Shock reflection with incident shock–wedge trailing-edge expansion fan interaction. *J. Fluid Mech.* **968**, A21.

Bai, C.-Y. & Wu, Z.-N. 2017 Size and shape of shock waves and slipline for mach reflection in steady flow. *J. Fluid Mech.* **818**, 116–140.

Chisnell, R.F. 1955 The normal motion of a shock wave through a non-uniform one-dimensional medium. *Proc. R. Soc. Lond.* A **232** (1190), 350–370.

Emanuel, G. 2001 Chapter 3.1 – shock waves in gases. In *Handbook of Shock Waves, Vol. 1* (ed. G. Ben-Dor, O. Igra & T. Elperin), pp. 185–262. Academic Press.

Gao, B. & Wu, Z.N. 2010 A study of the flow structure for mach reflection in steady supersonic flow. *J. Fluid Mech.* **656**, 29–50.

Glass, I.I. 1991 Over forty years of continuous research at UTIAS on nonstationary flows and shock waves. *Shock Waves* **1** (1), 75–86.

Hillier, R. 2007 Shock-wave/expansion-wave interactions and the transition between regular and mach reflection. *J. Fluid Mech.* **575**, 399–424.

Hornung, H.G. & Robinson, M.L. 1982 Transition from regular to mach reflection of shock waves. Part 2. The steady-flow criterion. *J. Fluid Mech.* **123**, 155–164.

Li, H. & Ben-Dor, G. 1996 Oblique-shock/expansion-fan interaction – analytical solution. *AIAA J.* **34** (2), 418–421.

Li, H. & Ben-Dor, G. 1997 A parametric study of mach reflection in steady flows. *J. Fluid Mech.* **341**, 101–125.

Moeckel, W.E. 1952 Interaction of oblique shock waves with regions of variable pressure, entropy, and energy. NASA *Tech. Rep.* NACA-TN-2725.

Mouton, C.A. & Hornung, H.G. 2007 Mach stem height and growth rate predictions. *AIAA J.* **45** (8), 1977–1987.

Nel, L. & Skews, B. 2019 Investigation of an expansion fan/shock wave interaction between high aspect ratio wedges. In *31st International Symposium on Shock Waves 1* (ed. A. Sasoh, T. Aoki & M. Katayama), pp. 783–790. Springer International Publishing.

Paramanantham, V., Janakiram, S. & Gopalapillai, R. 2022 Prediction of mach stem height in compressible open jets. Part 1. Overexpanded jets. *J. Fluid Mech.* **942**, A48.

Thara Reshma, I.V., Vinoth, P., Rajesh, G. & Ben-Dor, G. 2021 Propagation of a planar shock wave along a convex–concave ramp. *J. Fluid Mech.* **924**, A37.

Vuillon, J., Zeitoun, D. & Ben-Dor, G. 1995 Reconsideration of oblique shock wave reflections in steady flows. Part 2. Numerical investigation. *J. Fluid Mech.* **301**, 37–50.

Whitham, G.B. 1958 On the propagation of shock waves through regions of non-uniform area or flow. *J. Fluid Mech.* **4** (4), 337–360.

Yao, Y., Li, S.G. & Wu, Z.N. 2013 Shock reflection in the presence of an upstream expansion wave and a downstream shock wave. *J. Fluid Mech.* **735**, 61–90.

Zucrow, M.J. & Hoffmann, J.D. 1977 *Gas Dynamics, Volume 2: Multi-Dimensional Flow*. Wiley.